

# Instability and mesoscale eddy fluxes in an idealized 3-layer Beaufort Gyre

Pål E. Isachsen<sup>1,2</sup>, Noam Sebastian Vogt-Vincent<sup>3</sup>, Helen L. Johnson<sup>3</sup>, Johan  
Nilsson<sup>4</sup>

<sup>1</sup>Department of Geosciences, University of Oslo

<sup>2</sup>Norwegian Meteorological Institute

<sup>3</sup>Department of Earth Sciences, University of Oxford

<sup>4</sup>Department of Meteorology, Stockholm University

## Key Points:

- A 3-layer model is used to study instability and eddy dynamics over the continental slope in a wind-driven gyre
- The eddy field fluxes potential vorticity down-gradient in all three layers
- Linearized stability calculations are able to reproduce the qualitative features of the nonlinear fluxes

---

Corresponding author: Pål Erik Isachsen, [p.e.isachsen@geo.uio.no](mailto:p.e.isachsen@geo.uio.no)

## Abstract

We study the impacts of a continental slope on instability and mesoscale eddy fluxes in idealized 3-layer numerical model simulations. The simulations are inspired by and mimic the situation in the Arctic Ocean’s Beaufort Gyre where anti-cyclonic winds drive anti-cyclonic currents that are guided by the continental slope. The forcing and currents are retrograde with respect to topographic Rossby waves. The focus of the analysis is on eddy potential vorticity (PV) fluxes and eddy-mean flow interactions under the Transformed Eulerian Mean framework. Lateral momentum fluxes in the upper layer dominate over the actual continental slope where eddy form drag, i.e. vertical momentum flux, is suppressed due to the topographic PV gradient. The diagnosis also shows that while eddy momentum fluxes are up-gradient over parts of the slope, the total quasi-geostrophic PV flux is down-gradient everywhere. We then calculate the linearly unstable modes of the time-mean state and find that the most unstable mode contains several key features of the observed finite-amplitude fluxes over the slope, including down-gradient PV fluxes. When accounting for additional unstable modes, all qualitative features of the observed eddy fluxes in the numerical model are reproduced.

## Plain Language Summary

The ocean circulation in the Arctic is heavily influenced by the bottom bathymetry. Essentially, currents are steered to follow continental slopes and submarine ridges. This topographic steering makes transfer of properties across continental slopes difficult, thus partially isolating the deep basins from the continental shelves. Oceanic macroturbulence, or ‘mesoscale eddies’, are able to cross bottom bathymetry, but transport by these features are also hampered. In this study a simplified numerical model is used to learn about how bottom bathymetry impacts eddy transport in and out of the Beaufort Gyre, a wind-driven large-scale gyre in the Arctic Ocean’s Canada Basin. The gyre is the largest reservoir of fresh waters in the Arctic, and understanding how topography controls the export of this freshwater is thought to be of crucial importance if climate models are to properly simulate a future Arctic Ocean. The study shines light on some key aspects that the models need to consider to get transport across the continental slope right.

## 1 Introduction

A wide range of observational and modelling studies have shown that the large-scale ocean currents at high northern latitudes are heavily guided by bottom bathymetry (Orvik & Niiler, 2002; Koszalka et al., 2011; Isachsen et al., 2012). Certainly, the geostrophically-balanced bottom currents need to be. This is because the weak planetary vorticity gradient at high latitudes leaves the geostrophic flow nearly divergentless. This, in turn, means that the bottom vertical velocity—set up by flow up or down bathymetric slopes—must be the same order of magnitude as the vertical velocity at the sea surface, which is very small indeed. The geostrophic currents further up in the water column are less constrained. But rotation of the thermal wind shear away from the bottom flow does require a non-trivial organization of vertical velocities or ageostrophic buoyancy transport which is not always ensured (Schott & Stommel, 1978; Schott & Zantopp, 1980). So, in practice, even surface currents typically feel the continental slopes and ridge systems thousands of meters below.

The strong topographic steering of the large-scale geostrophic flow field then brings up the question of what processes are responsible for transport of water tracers and suspended material *across* topographic gradients. Flow in Ekman layers, both at the sea surface and at the bottom, can do so. But away from these frictional boundary layers property fluxes across continental slopes and over submarine ridges instead rely on temporal and/or spatial correlations between velocity and tracer fluctuations. Such fluctuations may be associated with organized wave phenomena, like tides, or with chaotic mo-

tions driven by wind fluctuations. In this study, however, we will focus on the role of the mesoscale eddy field which is as ubiquitous in the high north as it is in the rest of the world oceans. Even though the velocity field of mesoscale eddies is nearly geostrophic, smaller ageostrophic flow components can exchange both passive suspended material and active tracers like buoyancy and momentum across continental slopes. Eddy transport can thus impact the hydrography and large-scale currents themselves.

In the high north, such eddy-mean flow interactions have mostly been studied in the context of the Beaufort Gyre, a large-scale anti-cyclonic flow feature in the Canada Basin of the Arctic Ocean. Here, anti-cyclonic winds drive a surface Ekman convergence of freshwater toward the center of the basin. This lifts the sea surface and pushes down isopycnals there, driving anti-cyclonic geostrophic currents near the surface and, at the same time, a thermal wind shear that reduces these currents at depth. The convergent surface Ekman transport itself is thought to be compensated by divergent bottom Ekman currents, so that one can envision a secondary overturning circulation through the gyre, inward at the surface, downward in the center of the gyre and outward at the bottom. In steady state the stratification in the gyre is almost certainly controlled, in part, by local air-sea-ice fluxes and small-scale diabatic mixing (Zhang & Steele, 2007; Spall, 2013). But under the sheltering effect of the sea ice cover, mesoscale eddy transport is almost certainly key. Essentially, the available potential energy (APE) field associated with the inclined density field drives baroclinic instability and eddy bolus thickness fluxes which are thought to counter the wind-driven overturning circulation. And the sum of these two opposing overturning cells is the 'residual' circulation which actually advects tracers in and out of the gyre (Davis et al., 2014; Manucharyan & Spall, 2015; Manucharyan et al., 2016). On seasonal time scales, the momentum transfer from winds to ocean and thus the surface Ekman transport are modulated by the sea ice motion, in what has been termed the 'ice-ocean governor' (Meneghello et al., 2018). But integrated over long time scales, and in the limit of weak small-scale mixing, the lowest-order dynamics of the gyre appears to be reflecting this relatively simple balance between the opposing wind-driven and eddy-driven overturning circulations.

A potential problem with this model of Ekman–eddy residual overturning circulation arises from the fact that baroclinic instability is hampered by the presence of the continental slopes which confine the Beaufort Gyre. At a most basic level this can be understood from the inability of interior dynamics to compensate for the vertical velocities generated by an eddy-induced overturning that interacts kinematically with sloping bathymetry. In essence, topographic potential vorticity (PV) gradients hinder *any* cross-bathymetric flow, be it large-scale or meso-scale. A more rigorous theoretical starting point is offered by the 'topographic Eady model' of Blumsack and Gierasch (1972). This model, in which a linear bottom slope is added to the Eady model of baroclinic instability, predicts reduced growth rates and generally also reduced length scales over sloping bathymetry. But when tested in realistic situations the model generally overestimates topographic suppression (Trodahl & Isachsen, 2018). Key limitations of the Eady framework itself include its inability to account for internal PV thickness gradients in the middle of the water column as well as relative vorticity gradients and lateral momentum fluxes.

This last limitation appears to be most severe over continental slopes, as suggested by two idealized numerical studies of wind-driven flows over continental slopes by Wang and Stewart (2018) and Manucharyan and Isachsen (2019), hereafter referred to as WS18 and MI19, respectively. Both studies focused on so-called retrograde flows, where the winds drive currents that are in the opposite direction to topographic waves (such waves have the coast to their right in the northern hemisphere). And the MI19 study was motivated specifically by the Arctic Ocean Beaufort Gyre—whose anti-cyclonic mean flow is retrograde. These numerical studies confirm that eddy form stress, i.e. the vertical transfer of momentum which is a signature of active baroclinic instability, is greatly reduced over the continental slope. What the eddy field instead does in both of these simulations

is to transfer momentum laterally in the surface layers, away from the slope region and to a location just off the slope where the bottom is relatively flat. Here, an eddy driven jet is formed. And this jet is then baroclinically unstable, allowing the wind momentum to finally be transferred to the solid ground below.

So nature finds its way to tackle the problematic topographic PV gradient. But the above-mentioned studies also left some unanswered questions. First, the lateral momentum fluxes over the slope in these models were not down-gradient everywhere, so the eddy field was not the result of pure barotropic instability in the upper layers. In both sets of simulations there was also some indication of reversed eddy form stress and the formation of prograde flows over the lower parts of the slope. Thus, the mesoscale dynamics, at least over idealized retrograde slopes, appears to be associated with regions of both up-gradient buoyancy fluxes and up-gradient momentum fluxes. WS18 tried to interpret the observed behavior in their channel simulation in terms of down-gradient PV fluxes, to connect with theories of eddy-driven jets along topography (e.g. Bretherton & Haidvogel, 1976; Holloway, 1992; G. Vallis & Maltrud, 1993). Doing the analysis along a set of mid-depth isopycnals, they indeed found down-gradient PV fluxes over the slope regions. But the same diagnostics also gave indications of up-gradient PV fluxes in other parts of their model domain, notably over the flat continental shelf and deep basin. Whether this somewhat complex behavior is a real dynamical feature or an artifact of their analysis method remains a puzzle.

Secondly, one wonders how the observed finite-amplitude eddy fluxes, and especially the observed up-gradient fluxes, relate to the stability properties of the flow. Specifically, it seems natural to ask: can the observed fluxes be explained, at least qualitatively, by the eigenvectors of the linearly unstable modes of the large-scale background field? WS18 assessed linear stability numerically with a quasi-geostrophic 1D vertical mode model and observed clear indications of topographic suppression of unstable growth—as well as enhanced growth over flat regions off-shore. But, due to the limitations of the 1D framework, they were unable to properly account for background lateral vorticity gradients and thus investigate whether the linearly unstable modes contain a signature of the lateral momentum fluxes observed in the non-linear fields.

The present study picks up from the works of WS18 and MI19 by looking closer into the dynamics of unstable growth and eddy transport over retrograde continental slopes. To focus on the core issues, we simplify the approach even more and study nonlinear fluxes as well as linear stability in a 3-layer context, in a circular basin meant to very crudely mimic conditions in the Beaufort Gyre. By reducing the vertical resolution so drastically we limit the types of instability which may be reproduced, e.g. preventing surface-trapped small-scale eddy growth which is frequently observed in the Arctic Ocean halocline (e.g. Zhao et al., 2014). What the model will be able to represent, however, is the larger mesoscale eddies responsible for the deep overturning circulation in the basin and, it can be argued, for the adjustment of the main halocline (the adjustment of the density interface of a two-layer system will require a deep overturning). That such an eddy field should exist has been suggested by stability calculations from real hydrographic profiles (Meneghello et al., 2021) and also by recent satellite-based observations (Kubryakov et al., 2021). We nonetheless incorporate three layers instead of two, to allow for an examination of impacts of internal PV gradients, if there are any.

The specific issues to be addressed in this idealized 3-layer study are i) the impact of a retrograde continental slope on PV fluxes, including an investigation into PV diffusivities, and ii) the relationship between the observed fluxes and the linearly unstable modes of the background state in the model. In order to examine both lateral and vertical momentum exchanges by unstable modes, we study linear stability in a 2D context—in a plane crossing the mean hydrography and mean flow. As will be seen, even under the extreme simplification of 3 layers, the linear calculation is able to qualitatively re-

produce the key features observed in the full-complexity primitive equation studies mentioned above.

The manuscript starts with a description of the numerical model and the linear stability algorithm. The main results are then organized into a first part describing and analyzing the fully non-linear fields and then a second part discussing the linear stability of the flow. The study wraps up with a brief discussion of obtained results and conclusions.

## 2 Methods

### 2.1 Numerical model simulations

The model used is Aronnax (Doddridge & Radul, 2018a), an open-source idealized non-linear isopycnal model, set on a staggered C-grid. The model is configured with an explicit free surface and no-slip lateral boundary conditions on an f-plane (a reasonable approximation at this high latitude) with Coriolis parameter  $f = 1.456 \times 10^{-4} \text{ s}^{-1}$  (the value at  $90^\circ\text{N}$ ). The harmonic lateral friction coefficient is set to  $15 \text{ m}^2 \text{ s}^{-1}$  and the linear bottom drag coefficient set to  $2 \times 10^{-6} \text{ s}^{-1}$ , both small enough to allow vigorous eddy fields. The horizontal resolution is set to 5 km, compared to a first baroclinic deformation radius of about 11 km in all experiments, so the configuration is eddy-permitting. A time-step of 90 s is chosen as a compromise between model stability and computation time.

The domain consists of a circular basin representing the Beaufort Gyre and a rectangular 'nudging channel' meant to represent a connection to hydrographic conditions outside of the gyre. The basin radius is 750 km and the channel dimensions are  $500 \times 500$  km. In the nudging region, layer thicknesses are relaxed towards reference values (see below) within a timescale of 0.1 days. The very short nudging time scale ensures that thickness anomalies generated by the slope and basin dynamics are washed out within the nudging region.

A linear continental slope is used. In the model's Beaufort Gyre, i.e. in the circular basin, the total depth  $H$  is defined as:

$$H(r) = H_0 + H_1 \cdot \min\left(\frac{R-r}{L_s}, 1\right), \quad (1)$$

where  $r$  is the radial distance from the gyre centre,  $R$  is the gyre radius (750 km),  $L_s$  is the horizontal extent of the continental slope (variable, depending on the experiment; see below),  $H_0$  is the minimum depth (500 m) and  $H_1$  is the height of the slope (3500 m). The nudging channel has the same slope steepness but a rectangular geometry (see Fig. 1). Finally, we add random noise to the bathymetry to help instigate instability. Although white noise would do, we used perlin noise (Perlin, 1985) of amplitude 20 m for a slightly more realistic representation of a bumpy bottom.

The model has three isopycnal layers with interface reduced gravities  $g'_{12} = g\Delta\rho_{12}/\rho_0 = 0.024 \text{ m s}^{-2}$  and  $g'_{23} = g\Delta\rho_{23}/\rho_0 = 0.008 \text{ m s}^{-2}$ . The resting layer thicknesses of the two top layers are 80 m and 120 m, respectively, while the thickness of the third layer varies over the continental slope but is 3800 m in the center basin. These values are loosely based on the basin-margin T-S profiles from Lique et al. (2015) and also correspond fairly closely with the 3-layer configuration of Manucharyan and Stewart (2022). There is no explicit interface friction or diapycnal volume transport between layers.

Surface forcing is wind stress only (no buoyancy forcing). In the circular domain the stress is purely azimuthal and given by

$$\tau^\theta(r) = a \frac{r}{4} (2 - b^2 r^2), \quad (2)$$

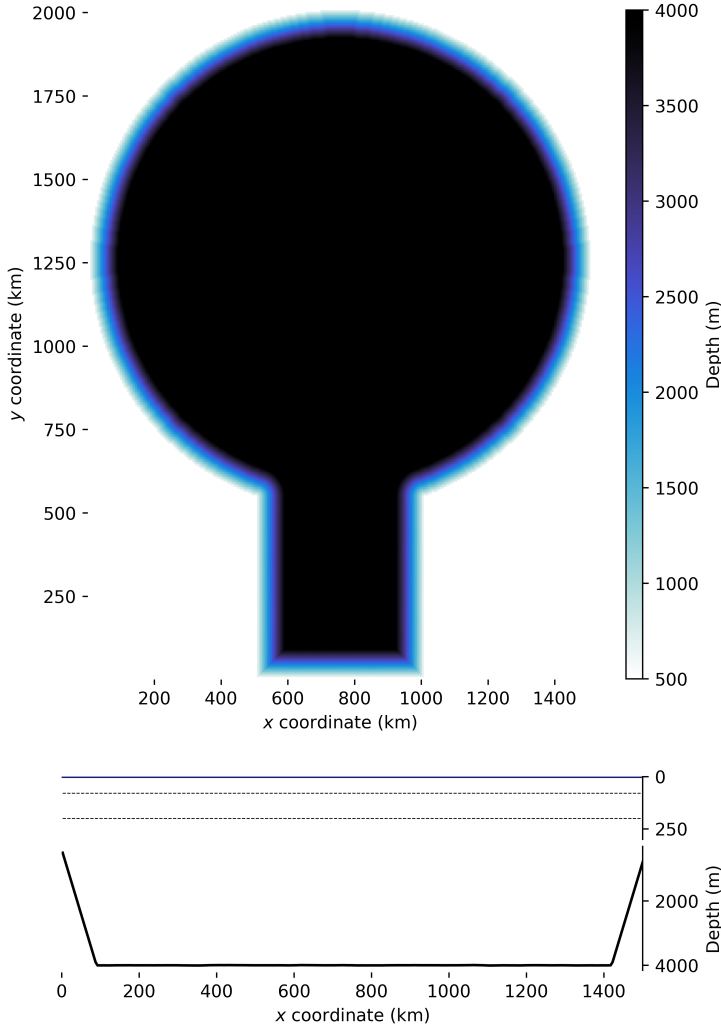


**Figure 1.** The bathymetry of one of the model runs that has continental slopes with 4% steepness. The top panel gives a plan view of the model bathymetry while the bottom panel shows a cross section through the center of the gyre, with dashed lines indicating the model layer interfaces at rest (note the break in scale).

where  $a$  is chosen such that the maximum anti-cyclonic wind stress curl is equal to  $0.02 \text{ N m}^{-2}$ , and  $b = 1/R$ . This profile is similar to that used in Davis et al. (2014) but avoids very large wind stress at the center of the gyre. The wind stress curl,

$$\nabla \times \tau = a (1 - b^2 r^2), \quad (3)$$

ramps down quadratically from maximum at the gyre centre to zero at the boundary of the circular basin. Outside the circular basin, the stress (in Cartesian directions) is given by

$$\tau^x = C \left( \frac{y}{r^2} \right), \quad (4)$$

$$\tau^y = C \left( -\frac{x}{r^2} \right), \quad (5)$$

where  $C$  is chosen to match the values at the boundary to the circular basin.

The wind stress is ramped up from zero to the maximum over a 20 year period (following a hyperbolic tangent profile) and held like this for another 40 years (for a total of 60 years), forming the spin-up. The model is then run for an additional 60 years over which relevant quantities are calculated and stored from 2-day snapshots. A classic time-based Reynold's decomposition is used to define 'mean' and 'eddy' variables, where the time-mean is taken over the last 60-year simulation period.

There are four distinct runs, each corresponding to a different continental slope width—corresponding to slope steepness of 1.5%, 2%, 4%, and 6%. One additional simulation with vertical sidewalls is also run, although this was not studied in detail.

## 2.2 Linear stability calculations

Since our idealized Beaufort Gyre is circular, the linear stability of the flow is evaluated in a 3-layer stacked shallow-water model cast in cylindrical coordinates  $(r, \theta, \text{layer})$ . So, for each layer we use the two inviscid momentum equations and the adiabatic layer thickness equation:

$$\frac{\partial u}{\partial t} + u \frac{\partial u}{\partial r} + \frac{v}{r} \frac{\partial u}{\partial \theta} - \frac{v^2}{r} - fv = -\frac{\partial \phi}{\partial r}, \quad (6)$$

$$\frac{\partial v}{\partial t} + u \frac{\partial v}{\partial r} + \frac{v}{r} \frac{\partial v}{\partial \theta} + \frac{uv}{r} + fu = -\frac{1}{r} \frac{\partial \phi}{\partial \theta}, \quad (7)$$

$$\frac{\partial h}{\partial t} = -\frac{1}{r} \frac{\partial (ruh)}{\partial r} - \frac{1}{r} \frac{\partial (vh)}{\partial \theta}. \quad (8)$$

Here  $u$  and  $v$  are the radial and azimuthal velocity components, respectively,  $f$  is the Coriolis parameter,  $\phi$  is the kinematic pressure and  $h$  is the layer thickness.

The pressures in the three layers are given by:

$$\phi_1 = g\eta, \quad (9)$$

$$\phi_2 = g\eta + g'_{12}\eta_{12}, \quad (10)$$

$$\phi_3 = g\eta + g'_{12}\eta_{12} + g'_{23}\eta_{23}, \quad (11)$$

where  $\eta$  is the sea surface displacement and  $\eta_{12}$  and  $\eta_{23}$  are the displacements of the two interfaces between the layers. Finally,  $g$  is the gravitational acceleration while  $g'_{12}$  and  $g'_{23}$  are the two reduced gravities (see above). The total layer thicknesses become

$$h_1 = H_1 + \eta(r, \theta, t) - \eta_{12}(r, \theta, t), \quad (12)$$

$$h_2 = H_2 + \eta_{12}(r, \theta, t) - \eta_{23}(r, \theta, t), \quad (13)$$

$$h_3 = H_3(r) + \eta_{23}(r, \theta, t), \quad (14)$$

where  $H_1$ ,  $H_2$  and  $H_3$  are layer thicknesses in the absence of motion. Note that  $H_3$  can vary in the radial direction to account for bottom topography.

We now linearize around a azimuthal-mean and time-mean azimuthal flow  $\bar{v}$  which is assumed to be in geostrophic balance with the sea surface and density field. So, for each layer, we write

$$u = u'(r, \theta, t), \quad (15)$$

$$v = \bar{v}(r) + v'(r, \theta, t), \quad (16)$$

$$[\phi, h, \eta] = [\bar{\phi}, \bar{h}, \bar{\eta}](r) + [\phi', h', \eta'](r, \theta, t), \quad (17)$$

where bars and primes indicate the background state and perturbations, respectively. The geostrophic background flow in layer  $j \in [1, 2, 3]$  is given by

$$f\bar{v}_j = \frac{\partial \bar{\phi}_j}{\partial r} \quad (18)$$



and the linearized equations for the perturbations (assumed to be much smaller than the background mean variables) in the same layer take the form

$$\frac{\partial u'_j}{\partial t} + \frac{\bar{v}_j}{r} \frac{\partial u'_j}{\partial \theta} - \frac{\bar{v}_j}{r} v'_j - f v'_j = -\frac{\partial \phi'_j}{\partial r}, \quad (19)$$

$$\frac{\partial v'_j}{\partial t} + u'_j \frac{\partial \bar{v}_j}{\partial r} + \frac{\bar{v}_j}{r} \frac{\partial v'_j}{\partial \theta} + \frac{\bar{v}_j}{r} u'_j + f u'_j = -\frac{1}{r} \frac{\partial \phi'_j}{\partial \theta}, \quad (20)$$

$$\frac{\partial h'_j}{\partial t} = -\frac{\partial (u'_j \bar{h}_j)}{\partial r} - \frac{\bar{h}_j}{r} u'_j - \frac{\bar{h}_j}{r} \frac{\partial v'_j}{\partial \theta} - \frac{\bar{v}_j}{r} \frac{\partial h'_j}{\partial \theta}. \quad (21)$$

The final step is to assume a wave solution in the azimuthal direction for all perturbations,

$$[u'_j, v'_j, \phi'_j, h'_j](r, \theta, t) = \text{Re} \left\{ [u_j, v_j, \phi, h_j](r) e^{i(l\theta - \omega t)} \right\}, \quad (22)$$

where  $i = \sqrt{-1}$  and the azimuthal wavenumber  $l$  is an integer larger than zero. Inserting into (19–21) gives the algebraic equation set

$$-i\omega u_j + il \frac{\bar{v}_j}{r} u_j - \frac{\bar{v}_j}{r} v_j - f v_j = -\frac{\partial \phi_j}{\partial r}, \quad (23)$$

$$-i\omega v_j + u'_j \frac{\partial \bar{v}_j}{\partial r} + il \frac{\bar{v}_j}{r} v_j + \frac{\bar{v}_j}{r} u_j + f u_j = -il \frac{1}{r} \phi_j, \quad (24)$$

$$-i\omega h_j = -\frac{\partial (u'_j \bar{h}_j)}{\partial r} - \frac{\bar{h}_j}{r} u'_j - il \frac{\bar{h}_j}{r} v'_j - il \frac{\bar{v}_j}{r} h_j. \quad (25)$$

In practice, we write the pressure and thickness perturbations in terms of sea surface and interface displacements, using (10) and (13), so that the equation set is in terms of  $u$ ,  $v$  and  $\eta$ . The equations for each layer are then discretized on a staggered grid in the radial direction, with  $v$  and  $\eta$  variables on the same points and  $u$  variables half-way between these. After applying the kinematic lateral boundary conditions  $u = 0$  in all three layers at the center of the gyre and at the side walls, (23–25) becomes an eigen problem (for each wavenumber  $l$ ) for eigenvalues  $\omega$  and eigenvectors  $[u_j, v_j, \eta_j]$ . We thus rotated the Cartesian model variables to a  $(r, \theta)$  grid, using a 3 km resolution in the radial direction to avoid any loss of resolution. All fields were then averaged azimuthally. Since the radius of our gyre is 750 km and the radial grid spacing is 3 km, we get 250  $v/\eta$ -points and 249  $u$ -points. Thus, for three layers, we get a  $2247 \times 2247$  eigen problem which is solved using the 'eig' function in Matlab. The imaginary part of eigenvalue  $\omega$  gives the growth rate of any given mode and we keep and study a small number of fastest-growing modes for analysis.

### 3 Results

#### 3.1 Finite-amplitude fields

##### 3.1.1 Overview

Figure 2 shows radial profiles of the temporally and azimuthally-averaged fields from one of the runs, BEAU004. This run, which has a continental slope with steepness 4% (a width of 58 km), will be the primary focus throughout the study. However, all runs contain similar qualitative features to BEAU004, except one run with vertical side walls. The upper and lower panels of the figure show the shape of the two isopycnals and the layer azimuthal velocities, respectively. The upper panel also shows the wind stress profile. As in all other figures, the inner 175 km of the basin are omitted since the focus is on the continental slope dynamics. The outer 25 km are also omitted since these contain wall effects.

We observe the expected depression of isopycnals towards the center of the basin and anti-cyclonic flow in all layers, with a progressively weaker flow at depth. But it's



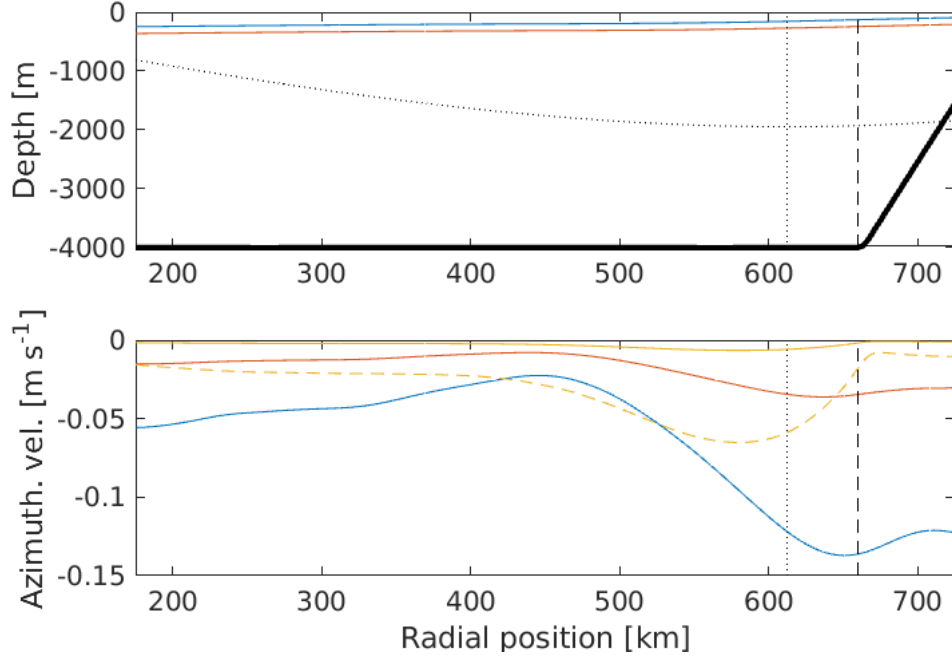


**Figure 2.** Temporally and azimuthally-averaged fields from the BEAU004 simulation (having a bottom slope of 4%). The top panel shows the isopycnals between layers 1 and 2 (blue) and layers 2 and 3 (red). Shown are also the bottom topography (thick solid line) and the wind stress profile (dotted black line, arbitrary units). The bottom panel shows the azimuthal velocity profiles for the top (blue), middle (red) and bottom (yellow) layers. The flow in the bottom layer is also shown after multiplication by a factor ten (dashed yellow line). In both panels vertical black lines indicate the position of the slope break (dashed) and the wind stress maximum (dotted). Note that the inner 175 km and outer 25 km of the domain have been excluded from this figure.

worth comparing the details of the radial flow profiles with what would be expected from a linear model of periodic flows around closed ambient PV contours (e.g. Gill, 1968; N st & Isachsen, 2003). In the absence of lateral momentum fluxes, the bottom stress would have to balance the wind stress at any radial position—so the flow strength, at least in the bottom layer, would closely track the wind strength. In a stratified fluid such transfer of wind momentum to the bottom layer would be mediated primarily by eddy form stresses, as small-scale turbulent stresses are assumed to be negligible away from the top and bottom boundary layers themselves. Figure 2 reveals a much more complex flow profile. The lower layer has a distinct flow maximum—a jet—which is offset off-shore from the wind stress maximum. And, importantly, the flow drops to near zero over the continental slope. Apparently, the vertical transfer of momentum to this layer all but vanishes there. This contrasts with the situation in a flat-bottom simulation that has vertical side walls (not shown). There the lower layer flow maximum coincides nearly perfectly with the wind stress maximum, as would be expected if eddy form stress is able to connect the top and bottom frictional layers and if lateral momentum fluxes thus become unimportant.

The flow profiles in the upper two layers also only mimic the wind profile in a very broad sense. Here too there is a jet, most visible in the top layer, which is slightly offset from the wind stress maximum in the direction of the boundary. As shown in Figure 3, in all the simulations the mean-flow maxima do not track the wind maximum but rather the configuration of the continental slope. Specifically, the upper layer maximum sits on top of the lower break of the continental slope while the lower layer maximum is always located slightly seaward of this position. This behavior is in agreement with the flows observed in the primitive equation simulations of both WS18 and MI19, but here we show that this is a robust feature over a range of bottom slopes. These results so far support the hypothesis that baroclinic instability, whose purpose is to transfer wind momentum down through the layers and into the solid earth below, is suppressed over the continental slope. Eddies instead first transfer the wind momentum in the upper layer offshore, to the location where the bottom slope vanishes. Seaward of that location, baroclinic instability can finally kick in to transfer the momentum to the frictional boundary layer at the bottom (see e.g. Fig. 2 in WS18).

To start examining this hypothesis, the lateral eddy momentum fluxes in the three layers for the BEAU004 run are shown in the upper panel of Figure 4. As for all analyses in this study, the calculation has been done in cylindrical coordinates where  $r$  and  $\theta$  are the radial coordinate and azimuthal angle, respectively, and  $u$  and  $v$  are the corresponding velocity components. The ‘eddy’ flux shown is thus  $\overline{u'v'}$ , where the overline indicates a combined azimuthal and temporal mean and the primes indicate deviations from such means. A positive value indicates a shore-ward flux of cyclonic momentum or, alternatively, a seaward flux of anti-cyclonic momentum. We see that, in the directly-forced top layer, eddies indeed transfer anti-cyclonic momentum seaward over and around the continental slope. There is an onshore flux of anti-cyclonic momentum in the deep basin, but this is quite weak. Finally, there is also a weak offshore flux in the middle layer but not in the lower layer.

Is the flow in the upper layer barotropically unstable? In helping to assess this, the lower panel of the figure shows the kinetic energy (KE) conversion rate:

$$C_{bt} = -\overline{hu'v'} \frac{\partial \bar{v}}{\partial r}, \quad (26)$$

A positive  $C_{bt}$  value indicates that azimuthal momentum is fluxed out of the mean flow, thus broadening any existing current and reducing mean-flow KE—the classic signature of barotropic instability. The diagnostic here, however, indicates a somewhat more complex picture, with momentum fluxed into the mean upper layer jet over the continental slope and out of the jet seaward of the slope. Eddies are therefore sharpening the jet, i.e. forming it, over the continental slope, and then broadening it over the flat regions

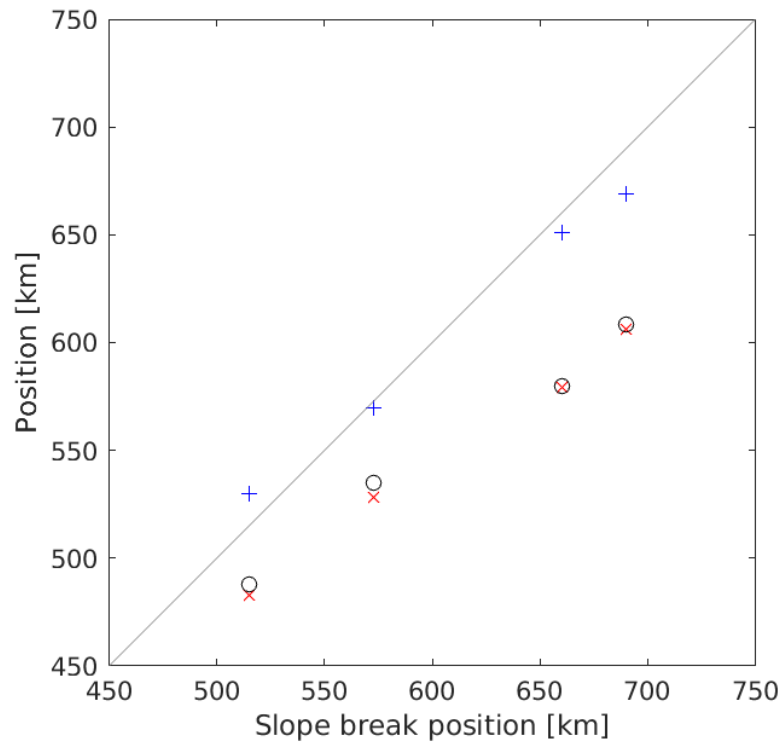


**Figure 3.** The positions of the velocity maximum in the top layer (blue crosses) and in the lower layer (red x'es) as a function of the position of the bottom of the continental slope. Also shown are the positions of the peak in the top layer eddy form drag (black circles).

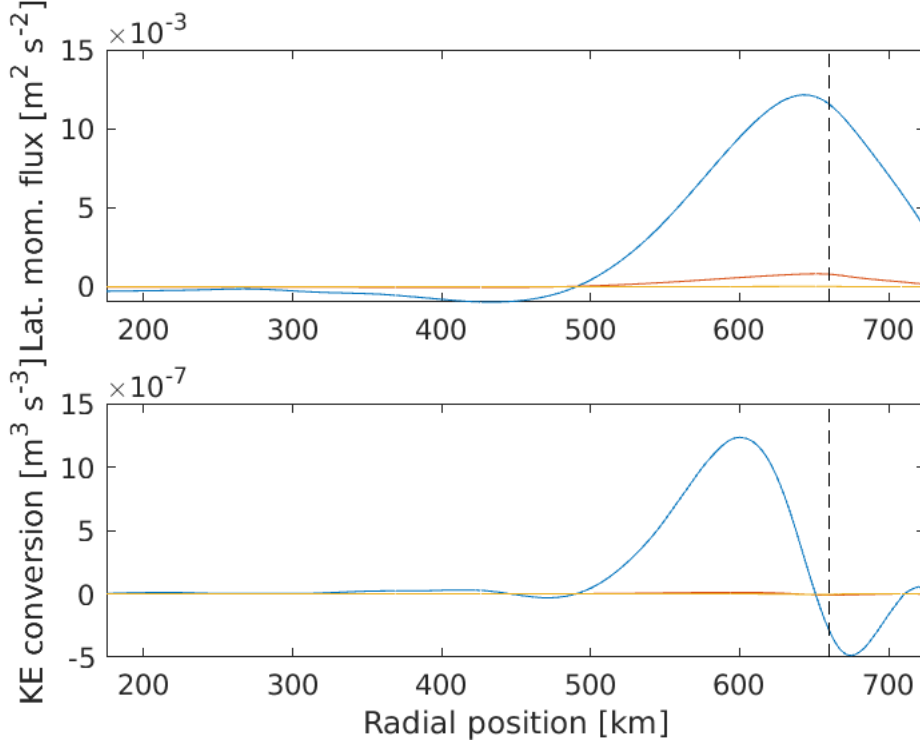


**Figure 4.** Upper panel: lateral eddy momentum fluxes for the BEAU004 simulation. Lower panel: the corresponding barotropic energy conversion rate. The solid lines indicate upper layer (blue), middle layer (red) and lower layer (yellow). Vertical dashed line indicates the position of the slope break.

further offshore. How this behavior relates to the linear stability of the flow will be examined in the next section. But first we continue to examine how the finite-amplitude eddy fluxes relate to the observed mean flow. For this, the key quantity of interest is the eddy momentum flux convergence, one part of which can be deduced from the radial derivative of the flux in the top panel of Figure 4, i.e. from the slope of the flux curve. This shows that the maximum convergence of lateral (anti-cyclonic) momentum flux in the top two layers takes place over the lower layer velocity maximum. It therefore appears that eddy fluxes may be driving the lower layer; but a more comprehensive picture will require actual diagnostics of vertical eddy momentum fluxes.

### 3.1.2 PV fluxes

The net impact of combined lateral and vertical eddy momentum fluxes can be captured in a thickness-weighted average of the azimuthal momentum equation. An approximate Transformed Eulerian Mean (TEM) expression for a given layer, in polar coordinates and assuming quasi-geostrophic (QG) scaling for the eddy motions, is (for a derivation in Cartesian coordinates, see G. K. Vallis, 2017, chapter 10):

$$\frac{\partial \bar{v}}{\partial t} + f \bar{u}^* = -\frac{1}{r} \frac{\partial}{\partial r} (r \overline{u'v'}) + \frac{1}{h} \left( \overline{\phi' \frac{1}{r} \frac{\partial \eta_t'}{\partial \theta}} - \overline{\phi' \frac{1}{r} \frac{\partial \eta_b'}{\partial \theta}} \right) + \frac{\bar{\tau}_t^\theta}{h} - \frac{\bar{\tau}_b^\theta}{h}, \quad (27)$$

where the overbar now only indicates an azimuthal average. Here  $\eta_t$  and  $\eta_b$  are top and bottom interfaces, and  $\tau_t^\theta$  and  $\tau_b^\theta$  represent small-scale turbulent vertical momentum fluxes through those interfaces (turbulent stresses). Note, finally, that  $\bar{u}^*$  in the Coriolis term

is the time-varying residual radial velocity of the layer,

$$\bar{u}^* = \bar{u} + \frac{\overline{u'h'}}{h}, \quad (28)$$

i.e. the effective mass transport velocity. So the lateral (radial) convergence of azimuthal momentum fluxes, in combination with a vertical convergence of interfacial form stress and/or turbulent stress, can accelerate the flow in the layer. Just like turbulent stresses  $\bar{\tau}^\theta$ , the form stresses  $\overline{\phi'(\partial\eta'/r\partial\theta)}$  can be interpreted as vertical (downward) fluxes of azimuthal momentum.

Under continued QG scaling, and using the periodicity of the domain, the convergence of the lateral momentum flux can be written in terms of an eddy vorticity flux, and the form stresses can be rewritten in terms of eddy advection of interface heights. The balance can thus be recast as

$$\frac{\partial\bar{v}}{\partial t} + f\bar{u}^* = -\overline{u'\zeta'} + \frac{f}{h} \left( \overline{u'\eta'_t} - \overline{u'\eta'_b} \right) + \frac{\bar{\tau}_t^\theta}{h} - \frac{\bar{\tau}_b^\theta}{h}, \quad (29)$$

where  $\zeta$  is relative vorticity. Finally, taking the difference of the two height advection terms gives

$$\frac{\partial\bar{v}}{\partial t} + f\bar{u}^* = -\overline{u'q'} + \frac{\bar{\tau}_t^\theta}{h} - \frac{\bar{\tau}_b^\theta}{h}, \quad (30)$$

where  $\overline{u'q'}$  is the QG PV flux,

$$\overline{u'q'} = \overline{u'\zeta'} - \frac{f}{h} \overline{u'h'}, \quad (31)$$

i.e. the QG approximation of the total eddy PV flux. The eddy forcing of the azimuthal mean flow of any given layer therefore consists of a lateral vorticity flux and a lateral thickness flux or, alternatively, a form drag. Figure 5 shows the long-term mean of the two contributions to the (negative) PV flux for each of the three layers in the same BEAU004 run. So we plot  $-\overline{u'\zeta'}$  and  $(f/h)\overline{u'h'}$  for each layer. A very robust signal, which is also present in all other runs (not shown), is the reduced eddy form drag in the top layer over the continental slope. By inspection of Figure 2, this is the region with the greatest thermal wind shear. Therefore, the region with the highest baroclinicity experiences a reduced form drag—a behavior which is consistent with the suspected suppression of baroclinic instability over a sloping bottom. The slope region is instead dominated by lateral eddy vorticity fluxes. As pointed out by MI19, these lateral fluxes tend to drive a cyclonic flow in the top layer or, more appropriately to our configuration here, to counter the anti-cyclonic flow set up by the wind forcing.

The eddy form drag increases in magnitude and dominates seaward of the continental slope, consistent with the notion that baroclinic instability can kick in here, transferring momentum to the layers below. The net effect is observed in Figure 2, i.e. a spin-up of the lower layer. In fact, the peak in upper layer eddy form drag coincides almost precisely with the center of the lower layer jet, as can be seen by comparing red crosses and black circles in Figure 3. It is also worth noting that the location of the maximum upper layer form drag corresponds to the largest lateral vorticity flux in the same layer. Eddy vorticity fluxes are therefore forcing the upper layer anti-cyclonically immediately off the continental slope, creating a jet there.

Fluxes in the middle layer are much weaker. But, more importantly, the eddy vorticity and thickness fluxes consistently oppose one another within this layer, tending to produce a very weak total PV flux. As a result, in this purely wind-driven setting, the middle layer appears to be rather dynamically inactive. In the lower layer, both fluxes all but vanish over the continental slope. The lower layer is therefore practically unforced there, at least by eddy fluxes. However, seaward of the slope the layer experiences a negative thickness flux, i.e. a negative form drag which again can be interpreted as a convergence of downward momentum fluxes. So it is here, off the continental slope, where the lower layer can finally be accelerated anti-cyclonically.

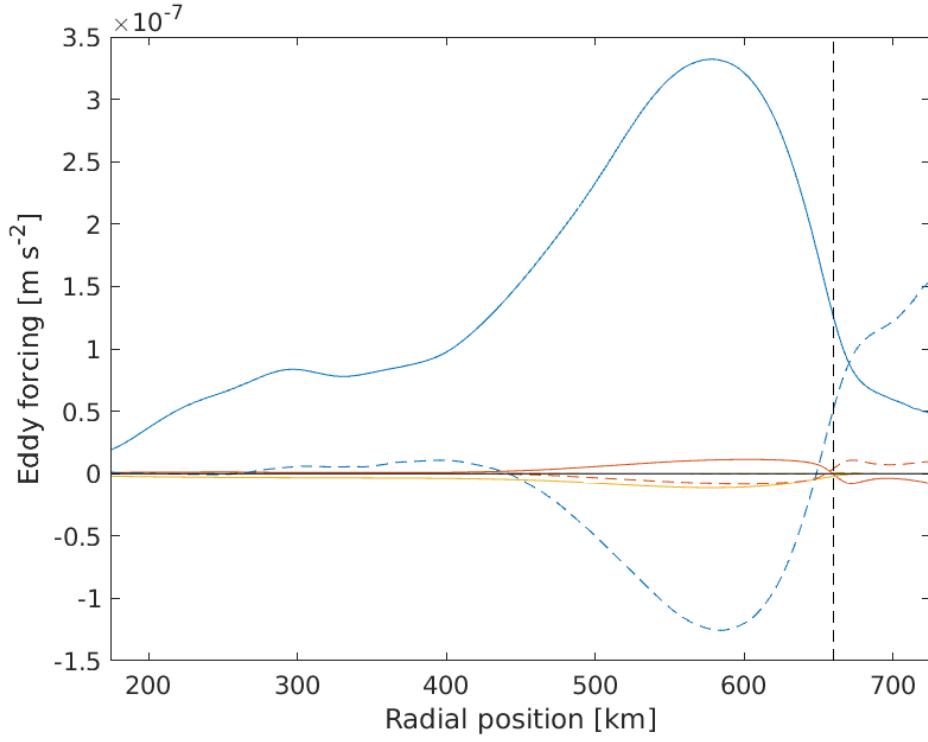


**Figure 5.** The two components of the negative eddy PV flux (see eqns. 30 and 31) in the BEAU004 run: negative vorticity flux  $-\overline{u'\zeta'}$  (dashed lines) and lateral thickness flux  $(f/\bar{h})\overline{u'h'}$  (solid lines) for each of the three layers (blue=top, red=middle and yellow=bottom). Vertical dashed line indicates the position of the slope break.

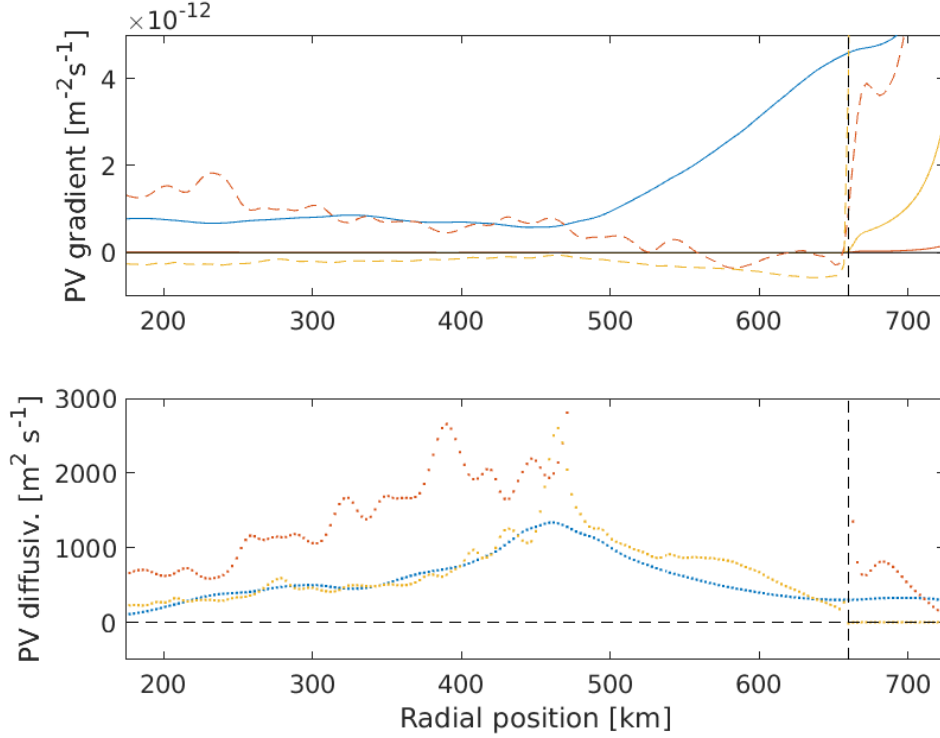


**Figure 6.** Top panel: the background PV gradient for each layer in the BEAU004 run; the dashed lines show the estimates multiplied by 100. Lower panel: PV diffusivities. Blue=top, red=middle and yellow=lower layer. The diffusivities in the middle layer oscillate between extremely large positive and negative values from about 470 km to the slope break. Vertical dashed line indicates the position of the slope break.

Adding the two flux components to form a total QG PV flux (not shown) reveals what can already be seen from Figure 5, namely that eddy PV fluxes decelerate the wind-driven anti-cyclonic flow in the top layer everywhere. These fluxes force the lower layer anti-cyclonically but, importantly, only seaward of the continental slope. Over the slope itself, the lower layer is practically unforced. Finally, the calculation reveals a near-zero eddy forcing of the middle layer everywhere. There are eddy momentum fluxes passing through this layer, but in the equilibrated state these are not convergent.

A PV eddy diffusivity can be estimated by first forming the total QG PV flux from the sum of the two components above and dividing by the background PV gradient. For units to match when merging QG and shallow-water formulations, the flux needs to be multiplied by the layer thicknesses. The PV gradient and the calculated diffusivity are in Figure 6. The background gradient will be discussed below, but the figure clearly shows that diffusivities in all three layers are positive nearly everywhere. Between 470 km and the slope break, diffusivities in the middle layer oscillate between extremely high positive and negative values. This behavior is tied to an extremely weak PV gradient in that layer which also switches sign there (see below). Except for this, diffusivities in all three layers take on similar forms and, interestingly, the upper and lower layer diffusivities are nearly equal. But, since the PV flux vanishes in the lower layer over the continental slope, the diffusivity there goes to zero.



## 3.2 The linear stability of the mean flow

### 3.2.1 Integral constraints and growth rates

We now turn to the linear stability properties of the background flow and ask whether the linearly unstable modes can explain at least some of the finite-amplitude fluxes discussed above. That they should do is in no way obvious, given the real possibility for nonlinear interactions to dominate the morphology of the equilibrated eddy field, resulting in e.g. an inverse energy cascade that brings energy away from the linear prediction.

Before conducting actual calculations that provide growth rates and modal structures of unstable waves, some intuition may be collected by re-examining the background PV gradients shown in Figure 6 in light of the general integral constraints which state that a necessary condition for instability is that the lateral PV gradient changes sign somewhere in the domain (see e.g. G. K. Vallis, 2017). We first note that the PV gradient does not change sign in the top layer, so the lateral momentum fluxes observed in that layer are likely not tied to pure barotropic instability (in agreement with the fact that momentum fluxes there are both up and down the background velocity gradient). The lateral gradient does change in the lower layer, right at the slope break, but background velocities here are small (Fig. 2) and lateral eddy momentum fluxes negligible (Fig. 4). This sign change is therefore unlikely to govern the stability properties significantly. A more notable feature is that the PV gradient does not change sign between the layers over the continental slope. This is indeed consistent with the prediction of the modified Eady model of Blumsack and Gierasch (1972), that very steep retrograde bottom slopes can stabilize the flow. There is, however, a sign change between the top and bottom layer immediately offshore of the slope break and then on-wards toward the basin center. As such, the integral considerations suggest that baroclinic instability is the primary mechanism at play. However, as suggested by the findings of the previous section, lateral momentum and vorticity fluxes are likely involved as well.

As above, the focus will be on the BEAU004 run. Using temporally and azimuthally-averaged fields from this simulation, the eigenvalue problem was solved for a set of integer azimuthal wavenumbers from 1 to 40 (wavenumber 1 corresponds to one wavelength spanning the circumference of the basin, etc.). For each wavenumber, the six fastest-growing unstable modes were then recorded, and the growth rates for these modes are plotted in Figure 7. There is some overlap between unstable modes, especially at low wavenumbers. But one 'lobe' of unstable modes stands out, producing the absolute fastest growth at  $l = 15$ . A second distinct lobe takes over at higher wavenumbers, with fastest growth at  $l = 31$ . As will be seen below, these two lobes both contribute to the observed PV fluxes over the model domain.

### 3.2.2 The $l = 15$ mode

The thickness and vorticity fluxes of the most unstable mode at  $l = 15$  are shown in Figure 8. These are to be compared with the corresponding finite-amplitude fluxes shown in Figure 5. Absolute magnitudes should not be compared, as these are arbitrary for the linear calculations (the eigenvector of each mode has norm one). But the spatial structure can be compared with that seen in the finite-amplitude fields. The linear prediction shows both similarities with and differences from the fully turbulent fields. The enhanced finite-amplitude vorticity flux in the top layer over the slope is not captured well by the linear mode, but both the suppression of thickness fluxes over the slope and an emergence and dominance of this contribution right off the slope are captured. It is also worth observing that the mode contains a near perfect cancellation between thickness flux and vorticity flux in the middle layer, reflecting the near-zero PV gradient in that layer. Importantly, the mode captures the negative thickness flux right off the slope in the lower layer, i.e. a negative form drag which tends to drive anti-cyclonic flow there.

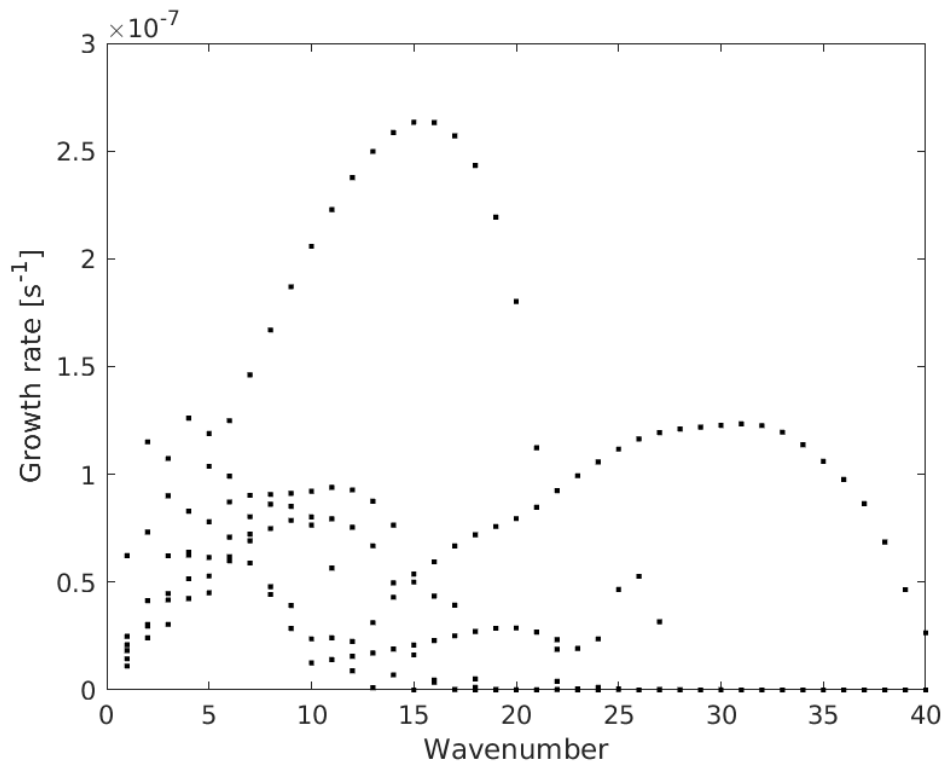


**Figure 7.** The growth rates of the six fastest-growing unstable modes in the BEAU004 simulation.

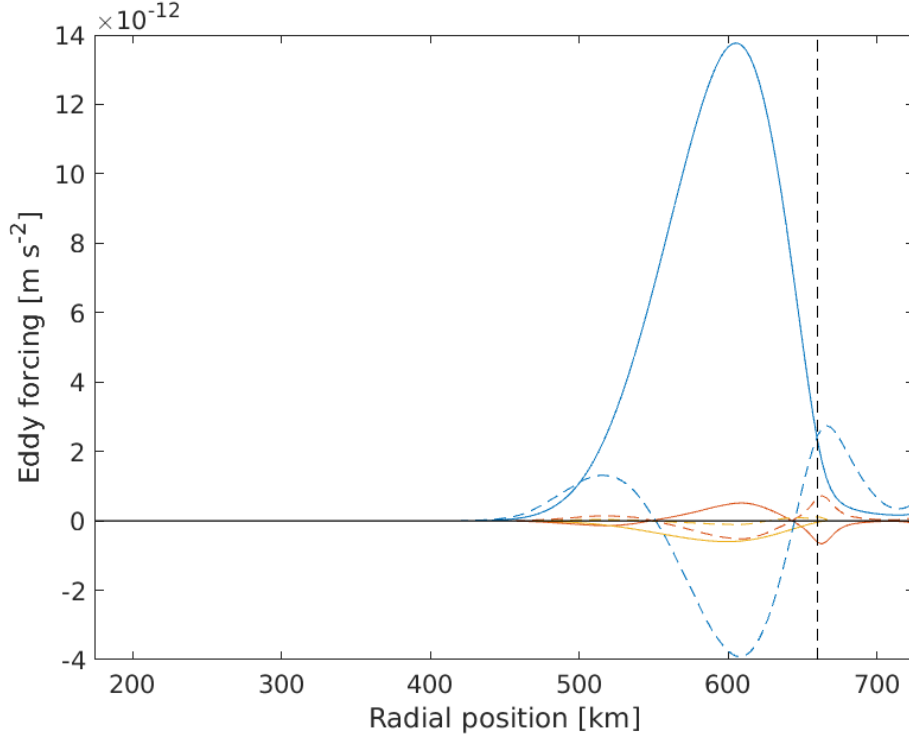


**Figure 8.** Same as Figure 5 but now calculated from the eigenvector of the fastest-growing unstable linear mode for wavenumber  $l = 15$ .

Figure 9 shows the total PV fluxes (the sum of the thickness and vorticity flux) and the calculated PV diffusivity of the mode (using the PV gradient plotted in Fig. 6). As for fluxes in the finite-amplitude field, the mode is hindering the wind-induced anti-cyclonic flow in the top layer and instead accelerating the lower layer. The diffusivities are positive in all three layers but noisy in the middle layer where both PV gradient and net fluxes all but vanish. As already seen above, the impact of this mode is maximal immediately offshore of the slope—where the lower layer jet is observed.

So this fastest-growing linear mode at wavenumber  $l = 15$  contains several of the essential characteristics of the finite-amplitude eddy fluxes around the continental slope. One might even be tempted to argue that, to a first approximation, the finite-amplitude fluxes are spread-out, or diffused, versions of the linear predictions. Such diffusion of the signal would be consistent with finite-amplitude eddy stirring of the active tracers in the problem. There are, however, notable discrepancies. Important to the focus here is that the linear mode has a near-zero form drag over the slope in the upper layer, whereas the finite-amplitude fields show a more gradual fall-off. The linear mode is also not able to reproduce the strong relative vorticity flux over the entire slope region.

The discrepancy in the deep basin further offshore is perhaps the most noticeable difference. There, the thickness fluxes and PV diffusivities vanish completely in the linear  $l = 15$  mode, whereas they remain finite in the fully-turbulent field. That there is an active thickness flux and form stress here, in the deep basin, is consistent with the sustained sign reversal of the PV gradient between the upper and lower layers (Fig. 6). Yet, these fluxes can not be related to the fastest-growing mode.

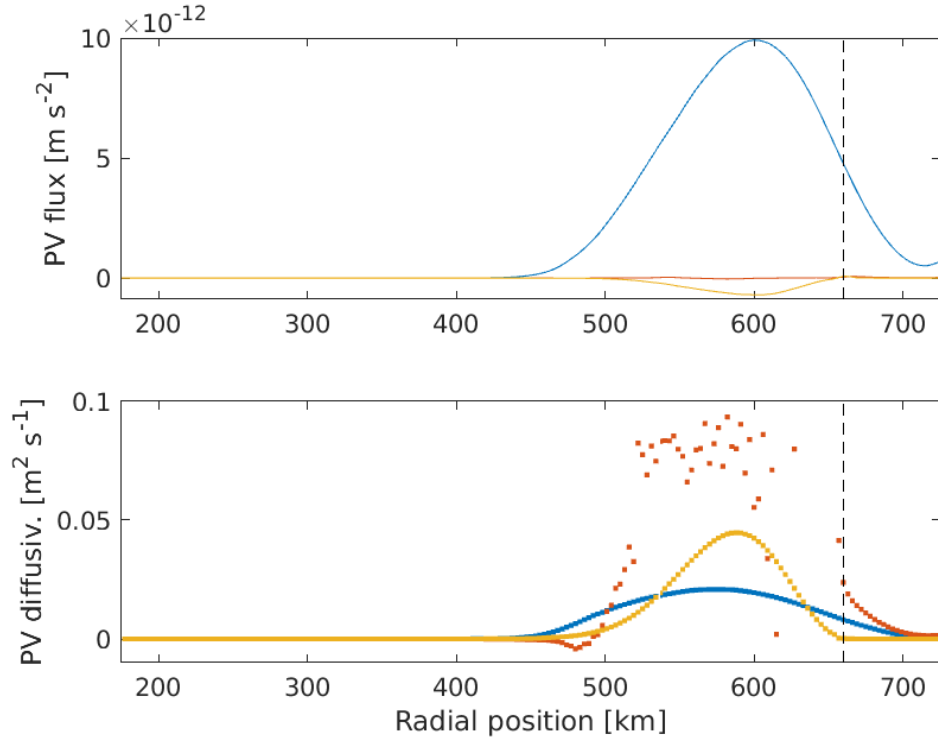


**Figure 9.** Top panel: the total QG PV fluxes calculated from the eigenvector of the fastest-growing unstable linear mode for wavenumber  $l = 15$ . Bottom panel: the corresponding PV diffusivities. Blue=top, red=middle and yellow=lower layer.

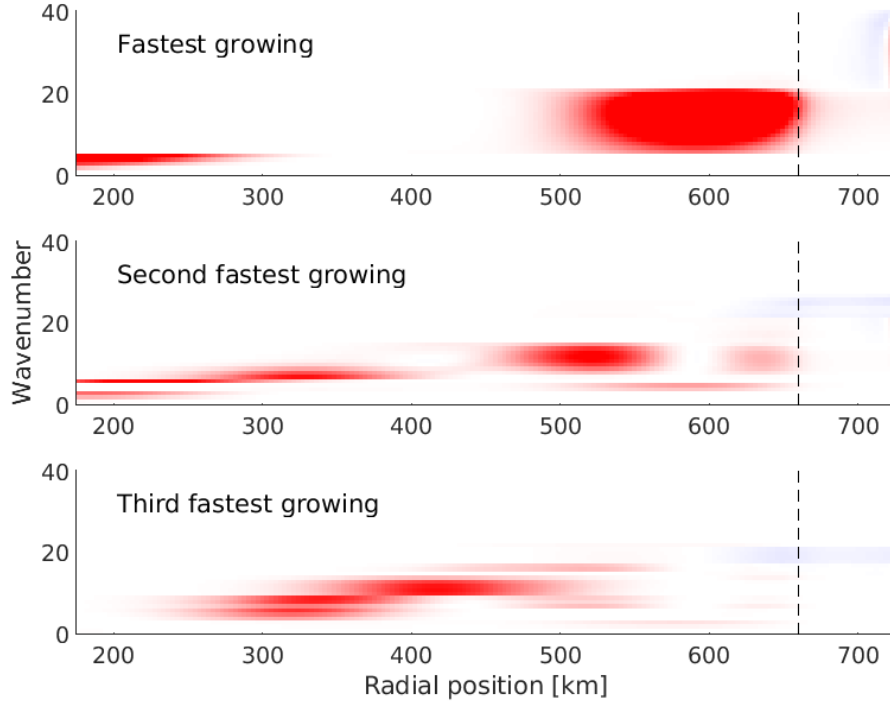


**Figure 10.** Lateral thickness fluxes  $(f/\bar{h})\overline{u'h'}$  in the upper layer calculated from the eigenvectors of the linear stability calculations, for mode 1 (fastest-growing; upper), mode 2 (second fastest-growing; middle) and mode 3 (third fastest-growing; lower). Magnitudes are arbitrary, but red and blue colors signify positive and values, respectively. Vertical dashed line indicates the position of the slope break.

### 3.2.3 Other unstable modes

Do other unstable modes contribute to the observed finite-amplitude fluxes, particularly over the upper parts of the continental slope and over the deep basin? Some indication can be had from Figures 10 and 11, which show thickness fluxes and negative vorticity fluxes in the top layer for the three fastest-growing linear modes at each wavenumber. Here, the estimates have been scaled by the growth rate for each mode. The resulting values (colors in the figure) should not be taken as indication of the exact level at which each mode would equilibrate if allowed to grow to finite amplitude. But scaling by the growth rate should nevertheless give some crude indication of the relative importance of the various modes.

As was already evident from Figure 7, the fastest-growing mode at  $l = 15$  is part of a dynamical feature which is unstable across a range of wavenumbers. Figures 10 and 11 suggest that this main lobe dominates both thickness and relative vorticity fluxes immediately offshore of the slope. It is also responsible for part of the vorticity flux over the slope itself, particularly over the lower part. However, as already seen above, the lateral vorticity flux of this mode falls to zero over the upper parts of the continental slope. There, the second lobe, which has fastest unstable growth for  $l > 20$ , dominates the vorticity flux.

What these calculations show, more generally, is that other unstable modes are responsible for both components of the PV flux over the deep basin away from the slope.

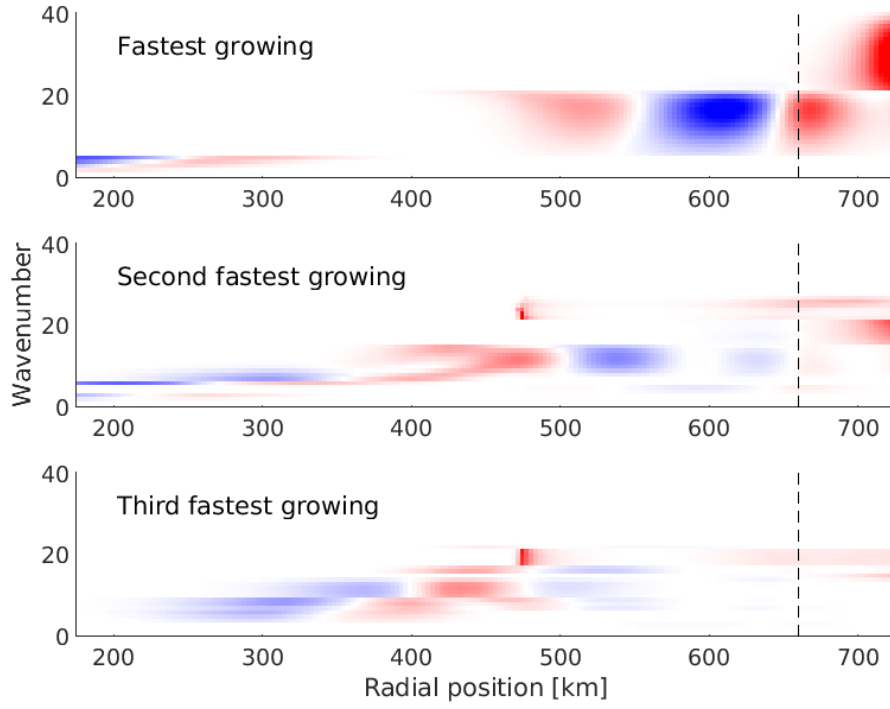


**Figure 11.** Negative lateral vorticity fluxes  $-\overline{u'\zeta'}$  in the upper layer calculated from the eigenvectors of the linear stability calculations, for mode 1 (fastest-growing; upper), mode 2 (second fastest-growing; middle) and mode 3 (third fastest-growing; lower). Magnitudes are arbitrary, but red and blue colors signify positive and negative values, respectively. Vertical dashed line indicates the position of the slope break.

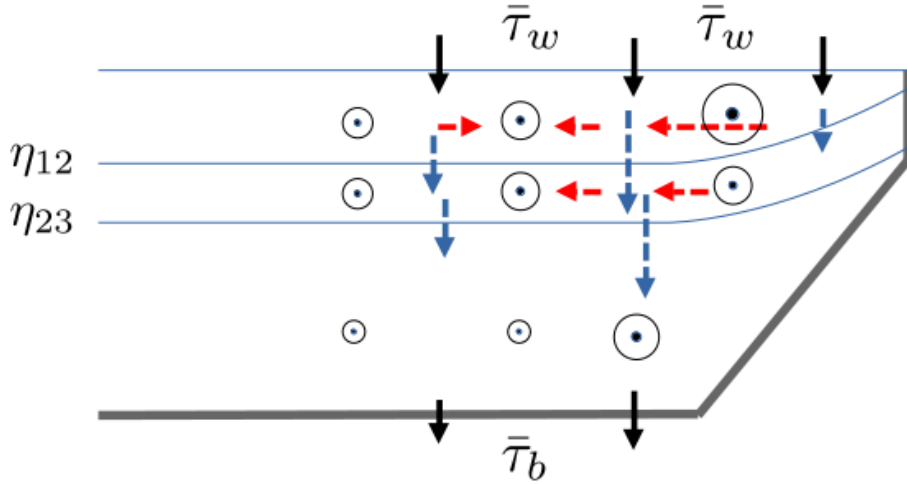


**Figure 12.** Sketch of eddy fluxes of anticyclonic momentum and the resulting azimuthal mean flow in the three layers. Black arrows show wind and bottom stresses, while red and blue dashed arrows show lateral momentum fluxes and form stresses, respectively.

This supports the interpretation that much of the finite-amplitude flux pattern seen in Figure 5 is a diffuse version of the linear mode fluxes—if one integrates over several unstable modes. One possible exception is the thickness flux over the continental slope; here all linear modes contain near-vanishing thickness fluxes, whereas the fully-turbulent fields reveal a more gradual fall-off. This important feature of the slope dynamics thus appears to be a truly finite-amplitude non-linear effect.

#### 4 Discussion and conclusions

Much of the dynamical behavior observed in this study can be seen as confirmation of the results presented by WS18 and MI19. However, by idealizing the model further, to three isopycnal layers only, we have been able to extract somewhat cleaner signals. Quite clearly, eddy form stress, i.e. the vertical transfer of the wind-induced anticyclonic momentum, is hampered over the model’s retrograde continental slope. But nature still finds a way, by transporting the wind momentum offshore to relatively flat regions where it can be efficiently transferred to lower layers and into the ground. The lateral eddy fluxes in upper layers are a direct result of the suppressed vertical momentum flux over the continental slope. The resulting pile-up of wind momentum over the slope sets up a strong lateral velocity shear between the flat and non-flat regions—which lateral shear instability tries to reduce. Figure 12 gives a rough sketch of the situation (see also Figure 2 of Wang & Stewart, 2018).

Perhaps the biggest advantage of the present 3-layer formulation is the ease with which one can investigate the linear stability properties of the background flow in a 2D framework. The very obvious role of lateral momentum fluxes seen in these model runs, as well as in the simulations of WS18 and MI19, points to the need for such 2D analysis. The classical 1D QG stability analysis conducted by WS18 is unable to pick up the dynamics responsible for the lateral fluxes. Earlier 2D stability analyses have typically used prescribed analytic background fields (e.g. Lozier & Reed, 2005; Ghaffari et al., 2018) and have thus not been able to compare directly with finite-amplitude fluxes. Here we have seen that several of the qualitative features of the observed PV flux in the model are reproduced by the fastest-growing unstable mode. But, importantly, other unstable



modes also contribute, both over the slope region and in the offshore deep basin. The linear calculations do not give any information on equilibrated energy levels and, hence, cannot reproduce the strength of eddy fluxes. But the fact that the observed finite-amplitude fluxes largely resemble diffuse versions of the linear predictions can be taken as a reminder that geophysical flows often adjust themselves into a marginally-unstable state at the wave-turbulence boundary, at least in the presence of a strong ambient PV gradient (e.g. Schneider & Walker, 2006).

As seen, even the 3-layer model was unnecessarily complex, as the middle layer in these simulations turned out to be dynamically passive. Indeed, separate 2-layer model simulations (not shown) contained all the key large-scale flow and eddy flux features discussed above. This is in agreement with the arguments that, in a purely wind-driven system, i.e. one that experiences barotropic forcing, there is no obvious mechanism which can produce internal PV gradients (Manucharyan & Stewart, 2022). So one may be tempted to conclude that a vertical discretization to two layers is valid for purely wind-driven systems. It is important to remember, however, that the real ocean also experiences buoyancy forcing at the surface where isopycnal layers outcrop, as well as diapycnal mixing in the interior. Both processes can give rise to interior thickness PV gradients that would add to the picture observed in these simulations.

In the real Arctic Ocean, interior layer thickness gradients do exist, as e.g. shown in Figure 9 of Meneghello et al. (2021). Observations and model studies from the central Beaufort Gyre also suggest that these gradients are dynamically responsible for the presence of sub-surface eddies that act to reduce those very gradients. These eddies have modest vertical and lateral scales, typically a few hundred meters and a few tens of kilometers, respectively. In comparison, the fastest-growing mode  $l = 15$  in our set-up will have a half-wavelength of about 135 km around bottom of the continental slope ( $r = 650$  km). So one is justified in questioning whether these simulations, as well as earlier similar model studies, are of any relevance for the situation in the Beaufort Gyre. It is worth noting, however, that most observations and theoretical studies of such smaller-scale halocline eddies have focused on the central gyre rather than on the continental slope along the rim of the gyre. And the possibility exists that the eddy dynamics is fundamentally different between these two regions. An indication of this may be a notable difference in vertical EKE profiles collected by four long-term mooring in the Beaufort Gyre. As shown in Figure 1 of Manucharyan and Stewart (2022), three moorings that are situated well within the gyre all reveal EKE maxima in the 50–250 m depth range, with rapid fall-off both above and below. In contrast, the last mooring which is situated over the continental slope off the Chukchi Plateau observed the highest EKE levels at the surface and, importantly, non-negligible energy levels at the bottom. The analysis of Manucharyan and Stewart (2022) do not reveal whether velocity fluctuations in upper and lower layers at this last mooring are correlated, i.e. whether the vertical EKE structure reflects a deep unstable mode. If that turns out to be the case, then one can anticipate that the lateral scales are also larger than those of the interior halocline eddies.

There is another peculiarity tied to the large lateral scales obtained in the present stability calculations. In the modified Eady theory of Blumsack and Gierasch (1972), the fastest-growing unstable mode over a retrograde slope has a lateral scale comparable to the internal deformation radius—which is of order 15 km in these simulations. Again, the fastest-growing linear mode found here is much larger than that. But the modified Eady problem does not tackle lateral shears and lateral momentum fluxes. As it turns out, the most unstable mode in our simulations takes on a scale which is approximately that of the width of the lateral shear zone. And this, in turn, appears to be set by the width of the continental slope. So it is possible that the internal deformation radius is no longer the most relevant length scale for the problem at hand—and neither along the Beaufort Gyre continental slope.

An interesting signal obtained in this layer model, both in the linear calculations and the fully-turbulent field, was the consistently down-gradient PV flux. The diagnosed PV diffusivity in the middle layer was, unsurprisingly, noisy due to the near-vanishing PV gradient there. But in all three layers the diffusivity was largely positive. Just as important to our dynamical understanding was the vanishing diffusivity and PV flux in the lower layer over the continental slope. So the lower layer was not forced over the slope and, as seen in Figure 2, had near-zero flow there. This last result is in slight disagreement with WS18 and MI19 who found weak but non-zero prograde currents over the lower parts of their continental slope. Eddy-driven prograde flows, bottom-trapped in stratified systems, are predicted by both minimum enstrophy and maximum entropy arguments (Bretherton & Haidvogel, 1976; Salmon et al., 1976; Venaille, 2012). We are unable to explain why prograde flows do not arise in the 3-layer simulations here, but note that such eddy-induced prograde flows—here in the opposite direction to the wind forcing—imply a local raising of APE near the bottom and thus depend on the energetics of the eddy field.

The most severe limitation of the study, in addition to the model’s low vertical resolution and inability to form small surface-trapped eddies, may be its neglect of irregular bottom variations, like corrugations and canyons. The possible excitation of standing topographic waves under the retrograde conditions we are studying here may give rise to additional form stresses that impact both buoyancy and momentum budgets to lowest order, as shown, by e.g. WS18. Bottom corrugations can also add form stress for prograde flows, but this does not involve energy accumulation into standing waves and thus appears to be of much lower importance (Bai et al., 2021). Given that the Arctic Ocean’s Beaufort Gyre is in fact retrograde, further investigation into this issue seems warranted.

If lateral momentum fluxes are still important, even if form stresses from standing waves are acting, then any topographically-aware mesoscale eddy parameterization for use in coarse-grained climate models needs to account for this. The results obtained here should be a reminder that a successful formulation needs to i) include lateral momentum fluxes and ii) be constrained to ensure down-gradient transport of full PV throughout the water column. Additionally, in the situation studied here with smooth topography, the parameterized PV flux should vanish over steep retrograde topography, a result which is also predicted by the modified Eady model of Blumsack and Gierasch (1972). But here, again, more work needs to be done in the situation where bottom corrugations are present—as they obviously are in the real ocean. Early assessments by Wang and Stewart (2020) suggest that standing waves contribute, but that eddy form stress is still reduced over retrograde slopes. This should not come as a surprise; *any* exchanges of semi-rigid water columns across sloping topography—the rigidity stemming from Earth’s rotation—should be hampered.

## Open Research Section

The isopycnal model used in this manuscript, Aronnax, is archived in a Zenodo repository (Doddridge & Radul, 2018a, 2018b). The code used to configure Aronnax for the experiments described in this manuscript and resulting model configuration files, the processed model output, and code used to carry out linear stability analysis, are archived in a separate Zenodo repository (Isachsen et al., 2023).

## Acknowledgments

This study was part of the TopArctic project funded by the Norwegian Research Council (grant 314826).

## References

- Bai, Y., Wang, Y., & Stewart, A. L. (2021). Does topographic form stress impede prograde ocean currents? *J. Phys. Oceanogr.*, *51*, 2617–2638. doi: 10.1175/JPO-D-20-0189.1
- Blumsack, S. L., & Gierasch, P. J. (1972). Mars: The effects of topography on baroclinic instability. *J. Atmos. Sci.*, *29*, 1081–1089.
- Bretherton, F., & Haidvogel, D. (1976). Two-dimensional turbulence over topography. *J. Fluid. Mech.*, *78*, 129–154.
- Davis, P. E. D., Lique, C., & Johnson, H. L. (2014). On the link between arctic sea ice decline and the freshwater content of the Beaufort Gyre: Insights from a simple process model. *J. Clim.*, *27*, 8170–8184. doi: 10.1175/JCLI-D-14-00090.1
- Doddridge, E., & Radul, A. (2018a). ‘aronnax’: An idealised isopycnal ocean model. *Journal of Open Source Software*, *3*(26), 592. Retrieved from <https://doi.org/10.21105/joss.00592> doi: 10.21105/joss.00592
- Doddridge, E., & Radul, A. (2018b, June). *edoddridge/aronnax: 0.2.0*. Zenodo. Retrieved from <https://doi.org/10.5281/zenodo.1290742> doi: 10.5281/zenodo.1290742
- Ghaffari, P., Isachsen, P. E., Nøst, O. A., & Weber, J. E. (2018). . *J. Phys. Oceanogr.*, *48*(11), 2761–2777. doi: 10.1175/jpo-d-17-0235.1
- Gill, A. (1968). A linear model of the Antarctic Circumpolar Current. *J. Fluid Mech.*, *32*, 465–488.
- Holloway, G. (1992). Representing topographic stress for large-scale ocean models. *J. Phys. Oceanogr.*, *22*(9), 1033–1046. doi: 10.1175/1520-0485
- Isachsen, P. E., Koszalka, I., & LaCasce, J. H. (2012). Observed and modeled surface eddy heat fluxes in the eastern Nordic Seas. *J. Geophys. Res. - Oceans*, *117*, 1–10. doi: 10.1029/2012JC007935
- Isachsen, P. E., Vogt-Vincent, N., Johnson, H., & Nilsson, J. (2023). *Supplementary datasets and code for: Instability and mesoscale eddy fluxes in an idealized 3-layer Beaufort Gyre*. Zenodo. Retrieved from <https://zenodo.org/doi/10.5281/zenodo.10152749> doi: 10.5281/ZENODO.10152749
- Koszalka, I., LaCasce, J. H., Andersson, M., Orvik, K. A., & Mauritzen, C. (2011). Surface circulation in the Nordic Seas from clustered drifters. *Deep-Sea Res. I*, *58*, 468–485. doi: 10.1016/j.dsr.2011.01.007
- Kubryakov, A. A., Kozlov, I. E., & Manucharyan, G. E. (2021). Large mesoscale eddies in the western Arctic Ocean from satellite altimetry measurements. *J. Geophys. Res. - Oceans*, *126*, e2020JC016670. doi: 10.1029/2020JC016670
- Lique, C., Johnson, H. L., & Davis, P. E. D. (2015). On the interplay between the circulation in the surface and the intermediate layers of the Arctic Ocean. *J. Phys. Oceanogr.*, *45*, 393–1409. doi: 10.1175/JPO-D-14-0183.1
- Lozier, M. S., & Reed, M. S. C. (2005). The influence of topography on the stability of shelfbreak fronts. *J. Phys. Oceanogr.*, *35*, 1023–1036.
- Manucharyan, G. E., & Isachsen, P. E. (2019). Critical Role of Continental Slopes in Halocline and Eddy Dynamics of the Ekman-Driven Beaufort Gyre. *J. Geophys. Res.*, *124*, 2679–2696. doi: 10.1029/2018JC014624
- Manucharyan, G. E., & Spall, M. A. (2015). Wind-driven freshwater buildup and release in the Beaufort Gyre constrained by mesoscale eddies. *Geophysical Research Letters*, *43*, 273–282. doi: 10.1002/2015GL065957
- Manucharyan, G. E., Spall, M. A., & Thompson, A. F. (2016). A theory of the wind-driven Beaufort Gyre variability. *Journal of Physical Oceanography*, *46*(11), 3263–3278.
- Manucharyan, G. E., & Stewart, A. L. (2022). Stirring of interior potential vorticity gradients as a formation mechanism for large subsurface-intensified eddies in the Beaufort Gyre. *J. Phys. Oceanogr.*, *52*, 3349–3370.

- Meneghello, G., Marshall, J., Lique, C., Isachsen, P. E., Doddridge, E., Campin, J.-M., ... Talandier, C. (2021). Genesis and decay of mesoscale baroclinic eddies in the seasonally ice-covered interior Arctic Ocean. *J. Phys. Oceanogr.*, *51*, 115-129. doi: 10.1175/JPO-D-20-0054.1
- Meneghello, G., Marshall, J., Timmermans, M.-L., & Scott, J. (2018). Observations of seasonal upwelling and downwelling in the Beaufort Sea mediated by sea ice. *Journal of Physical Oceanography*, *48*(4), 795-805.
- Nøst, O. A., & Isachsen, P. E. (2003). The large-scale time-mean ocean circulation in the Nordic Seas and Arctic Ocean estimated from simplified dynamics. *J. Mar. Res.*, *61*, 175-210. doi: 10.1357/002224003322005069
- Orvik, K. A., & Niiler, P. (2002). Major pathways of Atlantic water in the northern North Atlantic and Nordic Seas toward Arctic. *Geophys. Res. Lett.*, *29*(19). doi: 10.1029/2002GL015002
- Perlin, K. (1985). An image synthesizer. *ACM SIGGRAPH Computer Graphics*, *19*, 287-296. doi: 10.1145/325165.325247
- Salmon, R., Holloway, G., & Hendershott, M. (1976). The equilibrium statistical mechanics of simple quasi-geostrophic models. *J. Fluid Mech.*, *75*, 691-703.
- Schneider, T., & Walker, C. C. (2006). Self-organization of atmospheric macroturbulence into critical states of weak nonlinear eddy-eddy interactions. *J. Atmos. Sci.*, *63*, 1569-1586. doi: 10.1175/JAS3699.1
- Schott, F., & Stommel, H. (1978). Beta-spirals and absolute velocities in different oceans. *Deep-Sea Res.*, *25*, 961-1010.
- Schott, F., & Zantopp, R. (1980). On the effect of vertical mixing on the determination of absolute currents by the beta spiral method. *Deep-Sea Res.*, *27*, 173-180.
- Spall, M. A. (2013). On the Circulation of Atlantic Water in the Arctic Ocean. *J. Phys. Oceanogr.*, *43*, 2352-2371. doi: 10.1175/JPO-D-13-079.1
- Trodahl, M., & Isachsen, P. E. (2018). Topographic influence on baroclinic instability and the mesoscale eddy field in the northern north atlantic ocean and the nordic seas. *Journal of Physical Oceanography*, *48*(11), 2593-2607. doi: 10.1175/JPO-D-17-0220.1
- Vallis, G., & Maltrud, M. (1993). Generation of mean flows and jets on a beta plane and over topography. *J. Phys. Oceanogr.*, *23*, 1346-1362.
- Vallis, G. K. (2017). *Atmospheric and oceanic fluid dynamics: Fundamentals and large-scale circulation* (2nd ed.). Cambridge, U.K.: Cambridge University Press.
- Venaille, A. (2012). Bottom-trapped currents as statistical equilibrium states above topographic anomalies. *J. Fluid Mech.*, *669*, 500-510. doi: 10.1017/jfm.2012.146
- Wang, Y., & Stewart, A. L. (2018). Eddy dynamics over continental slopes under retrograde winds: Insights from a model inter-comparison. *Ocean Modelling*, *121*, 1-18. doi: 10.1016/j.ocemod.2017.11.006
- Wang, Y., & Stewart, A. L. (2020). Scalings for eddy buoyancy transfer across continental slopes under retrograde winds. *Ocean Modelling*, *147*, 101579. Retrieved from <https://www.sciencedirect.com/science/article/pii/S1463500319301775> doi: <https://doi.org/10.1016/j.ocemod.2020.101579>
- Zhang, J., & Steele, M. (2007). Effect of vertical mixing on the Atlantic Water layer circulation in the Arctic Ocean. *J. Geophys. Res.*, *112*(C04S04). doi: 10.1029/2006JC003732
- Zhao, M., Timmermans, M.-L., Cole, S. T., Krishfield, R., Proshutinsky, A., & Toole, J. M. (2014). Characterizing the eddy field in the Arctic Ocean halocline. *J. Geophys. Res. Oceans*, *119*, 8800-8817. doi: 10.1002/2014JC010488